The dynamics of wind-driven intraseasonal variability in the equatorial Indian Ocean

Motoki Nagura[1] and Michael J. McPhaden[2]

Received 26 June 2011; revised 18 November 2011; accepted 22 November 2011; published 1 February 2012.

[1] Variability in the equatorial Indian Ocean on intraseasonal time scales (defined as periods of 30–110 days) is investigated using satellite and in situ observations and a simple analytical linear long-wave equatorial β-plane model. Despite the extreme simplicity of the model, which includes just the two gravest baroclinic mode Kelvin waves and first meridional mode Rossby waves, simulated surface zonal velocity and sea surface height compare very well with observations. Both observations and model are characterized by a red shift in the velocity spectrum relative to the wind forcing spectrum, which is attributable to a combination of factors, including (1) the near resonant excitation of Kelvin waves by eastward propagating winds, (2) constructive interference between wind-forced waves and Rossby waves reflected from the eastern boundary, and (3) the favored excitation of low-frequency waves whose zonal wavelengths are long compared to the zonal fetch of the wind. We decomposed variability in two broad period bands, namely, 30–70 days and 70–110 days, for detailed analysis. At periods of 30–70 days, zonal velocity tends to be stationary in the directly forced region along the equator owing to the competing contributions of Kelvin and Rossby waves. In contrast, at 70–110 day periods, zonal velocity propagates westward despite eastward propagation of zonal wind stress because of the combined influence of eastern boundary generated and wind-forced Rossby waves. Kelvin waves reflected from the western boundary are negligibly small, indicating that basin mode resonances are not prominent as has been previously suggested.

Citation: Nagura, M., and M. J. McPhaden (2012), The dynamics of wind-driven intraseasonal variability in the equatorial Indian Ocean, *J. Geophys. Res.*, *117*, C02001, doi:10.1029/2011JC007405.

1. Introduction

[2] Vigorous intraseasonal zonal velocity and sea surface height (SSH) variations have been observed in the equatorial Indian Ocean [*Luyten and Roemmich*, 1982; *McPhaden*, 1982; *Reverdin and Luyten*, 1986; *Reppin et al.*, 1999; *Han et al.*, 2001; *Brandt et al.*, 2003; *Han*, 2005; *Masumoto et al.*, 2005; *Fu*, 2007; *Iskandar and McPhaden*, 2011]. While intraseasonal variability in the western Indian Ocean is associated with dynamical instability of the large-scale flow field near the western boundary [*Sengupta et al.*, 2001], variability in the central and eastern Indian Ocean has been considered a consequence of atmospheric forcing. It is also known that spectra for oceanic velocity and SSH exhibit a red shift toward lower frequencies compared to zonal wind stress forcing. In particular, winds have strong power at periods of 30–50 days, while the oceanic variables have more power at periods of 50–90 days [*Han et al.*, 2001, 2011; *Senan et al.*, 2003; *Han*, 2005; *Fu*, 2007; *Sengupta et al.*, 2007].

[3] Much modeling and diagnostic work has been done on intraseasonal variability in the Indian Ocean, but there are still some outstanding issues. For example, near-equatorial velocity variability has not yet been fully described, which limits our ability to understand the fundamental processes that govern that variability. Here we will use the satellite-based Ocean Surface Current Analysis Real time (OSCAR) [*Bonjean and Lagerloef*, 2002] surface velocity analysis and multiyear-long equatorial mooring records from the Research Moored Array for African-Asian-Australian Monsoon Analysis and Prediction (RAMA) [*McPhaden et al.*, 2009] to characterize both the temporal and spatial structures of intraseasonal velocity variations.

[4] We also use a simple analytical model validated by these observations to examine how equatorial wave dynamics affect the observed variability. The model is a linear long-wave model on an equatorial β-plane involving just the first two baroclinic mode Kelvin and first meridional mode Rossby waves. This has successfully been applied to studies of the mean seasonal cycle and interannual variability in the Indian Ocean [*Nagura and McPhaden*, 2010a, 2010b]. The model is realistic enough to allow for a direct comparison

[1]Application Laboratory, Japan Agency for Marine-Earth Science and Technology, Yokohama, Japan.
[2]Pacific Marine Environmental Laboratory, National Oceanic and Atmospheric Administration, Seattle, Washington, USA.

0148-0227/12/2011JC007405

with observations of simulated ocean variability forced by complex wind patterns on intraseasonal time scales. With this model, we will examine the hypothesis that basin mode resonance is responsible for the generation of intraseasonal oscillations in the equatorial Indian Ocean, particularly at periods of 90 days [*Han et al.*, 2001, 2011; *Han*, 2005; *Fu*, 2007]. Basin modes exist when the period of the wind forcing is similar to that of a natural basin mode oscillation, which involves the constructive interference of directly wind forced waves with reflected Kelvin waves generated at the western boundary and reflected Rossby waves generated at the eastern boundary.

[5] Past studies on intraseasonal variability in the Pacific Ocean pointed out that the spatial and temporal characteristics of intraseasonal wind forcing are crucial factors in the excitation of oceanic waves. *Kessler et al.* [1995] modeled intraseasonal zonal wind forcing in the equatorial Pacific Ocean as a standing oscillation and found that waves are preferentially excited when their zonal wavelengths are long compared to the zonal fetch of the wind. For nondispersive waves, this favors the lower-frequency part of the response spectrum since wind work damps higher-frequency, shorter-wavelength waves as they are traverse the forcing region. This preferential excitation of waves at longer periods leads to a reddening of the response spectrum at intraseasonal time scales in the Pacific Ocean. *Hendon et al.* [1998] focused on eastward migration of intraseasonal winds observed in the Pacific Ocean and pointed out that oceanic waves are resonantly excited if they have a phase speed similar to that of the propagating winds. On the other hand, the details of wind forcing patterns and how they affect observed variability in the Indian Ocean have not yet been thoroughly examined on intraseasonal time scales.

[6] Here we will use high-quality QuikSCAT (QSCAT) satellite winds to force our model. These winds are much higher quality than reanalysis winds used by *Han et al.* [2001] and *Han* [2005], which will allow us to look in more detail at hypothesized basin mode resonances and factors responsible for the observed red shift in zonal velocity relative to the wind forcing. *Sengupta et al.* [2007] and *Han et al.* [2011] also forced dynamical models with QSCAT satellite winds, but their analysis of wave dynamics relied on experiments with prescribed idealized winds.

[7] The rest of the paper is organized as follows. Section 2 introduces the observational data. In sections 3 and 4, we summarize the formulation of our numerical model and validate it against observations. Section 5 describes and diagnoses the wind forced ocean response in zonal velocity and sea level. Section 6 summarizes our main conclusions and offers perspectives on their importance.

2. Observations

[8] We force our model (described in section 3) with surface winds obtained from QSCAT satellite measurements, which are available from 19 July 1999 to 12 October 2009 on 0.5° × 0.5° grid. We computed daily zonal wind stresses from wind velocities using a drag coefficient of 1.43×10^{-3} and air density of 1.225 kg m^{-3} [*Weisberg and Wang*, 1997]. Background stratification in the model is defined using Argo float observations provided by the Institut français de recherche pour l'exploitation de la mer (IFREMER) Coriolis Data Center. The Coriolis data center provides temperature and salinity observations on 0.5° × 0.5° grid from the sea surface to 2000 m depth.

[9] Model results are compared with in situ velocity observations from upward looking acoustic Doppler current profilers (ADCPs) deployed on subsurface moorings as part of RAMA [*McPhaden et al.*, 2009]. We use data from a four year record in the center of the basin at 0°, 80.5°E (27 October 2004 to 17 October 2008), which we extended to August 2009 via interpolating two shorter records at 0°, 83°E (8 August 2008 to 25 August 2009) and 0°, 78°E (11 August 2008 to 28 August 2009) to 80.5°E. The error involved in this interpolation is negligible for our purposes [*Nagura and McPhaden*, 2010b]. The ADCP provides daily averaged velocity data from near the sea surface to a depth of 175 m with 5 m resolution. Data at depths shallower than 35 m are contaminated by acoustic signals reflected from the sea surface and are discarded and replaced with values linearly extrapolated from deeper levels. The error involved in this vertical extrapolation is relatively small on the intraseasonal time scales compared to direct velocity measurements from a point current meter at 10 m depth (correlation of 0.97 and root mean square difference of 0.05 m s^{-1} for 30–110 day periods). Similarly, ADCP velocities extrapolated to 15 m depth also compared well with the OSCAR analysis.

[10] Satellite observations are used to characterize the space/time evolution of intraseasonal variability and to validate model results. SSH observations are obtained from satellite altimetry provided by Archiving, Validation, and Interpretation of Satellite Oceanographic Data (AVISO) [*Ducet et al.*, 2000]. This product is available with weekly resolution on a 0.25° × 0.25° resolution grid from 14 October 1992 to 4 November 2009. The OSCAR velocity analysis [*Bonjean and Lagerloef*, 2002] is available as 5 day averages on a 1° × 1° grid for the period of 21 October 1992 to 7 July 2010, and representative of flow in the mixed layer at a 15 m depth. This product is derived from satellite altimetry measurements of ocean surface height, surface winds and sea surface temperature, using a diagnostic model of ocean currents based on frictional and geostrophic dynamics.

3. Model

[11] The model is a wind-driven, linear, continuously stratified long-wave ocean model on an equatorial β-plane. This model has been successfully applied to circulation studies in the equatorial Indian Ocean [*Nagura and McPhaden*, 2010a, 2010b], the equatorial Pacific Ocean [*Yu and McPhaden*, 1999; *McPhaden and Yu*, 1999; *Zhang and McPhaden*, 2006] and the equatorial Atlantic Ocean [*Foltz and McPhaden*, 2010a, 2010b]. *Yu and McPhaden* [1999] describe the model in detail and the basic equations of the model are shown by *Nagura and McPhaden* [2010a, Appendix A]. *Sengupta et al.* [2007] demonstrated that a linear momentum balance applies in the equatorial Indian Ocean for intraseasonal variability simulated in an ocean GCM; and *Han et al.* [2011] found very similar intraseasonal variations in a continuously stratified Indian Ocean model linearized about a state of rest compared to those in a GCM. These results show that wind-driven intraseasonal variability in the Indian Ocean is dominated by linear dynamics, and that

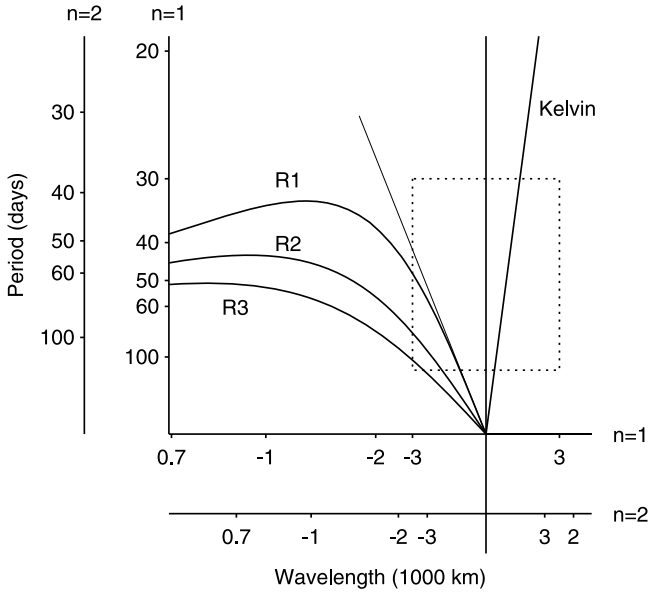

Figure 1. Dispersion relation for equatorial Kelvin waves and low-order meridional mode Rossby waves (R1, R2, R3) for the first (n = 1) and the second (n = 2) baroclinic modes. The horizontal axis is drawn in units of 1000 km. The dotted square shows how typical spatial and temporal scales for intraseasonal variability would map onto the first baroclinic mode. Spatial scales are obtained from wind forcing shown in Figures 8 and 10. The thin line denotes the long-wave approximation for nondispersive first meridional mode Rossby waves.

nonlinear interactions with lower-frequency currents can for the most part be neglected.

[12] We used mean density stratification defined from the Coriolis Data Center Argo float analysis to define the background state of rest in the model. Potential density computed from Argo temperature and salinity is averaged over the region of 15°S–15°N and 40°E–100°E and the period of 2004 to 2008, and extrapolated to 4000 m depth. The resultant profile is used as the background state. *Nagura and McPhaden* [2010a] showed that results are not sensitive to variations in the area used to define the mean density profile.

[13] Velocity and pressure variability in the model is decomposed into vertical modes and meridional modes, assuming a flat bottom ocean. Vertical mode decomposition indicates wave speeds of 2.50, 1.55, 0.99 and 0.74 m s^{-1} for the first four baroclinic modes, respectively, consistent with results of similar calculations in earlier studies [*Reverdin*, 1987; *Clarke and Liu*, 1993; *Han*, 2005]. Meridional mode decomposition yields equatorial Kelvin waves and long Rossby waves which, in the long-wave limit, are nondispersive. The zonal wavelengths and periods of these equatorial wave modes are illustrated in the dispersion diagram (Figure 1) [see also *Philander*, 1990]. For the time and zonal scales we are interested in (periods of 30–110 days and zonal wavelengths of 1000s of kilometers), Kelvin and first meridional mode Rossby waves will dominate the solutions. Our model does not represent short zonal scale intraseasonal Rossby waves accurately because these waves are dispersive. However, because we are interested in the large-scale response to wind forcing, these waves do not play a significant role as will become evident in our comparison of the model results to observations.

[14] We obtain solutions by projecting the zonal wind forcing onto each vertical and meridional mode and integrating the projected forcing with the method of characteristics. The grid intervals are 2° and 4.8 h in longitude and time, respectively. The integration period is for 19 July 1999 to 17 November 2009. The damping coefficient is formulated as A/c_n^2, where A is an arbitrary constant and c_n is the wave speed of the baroclinic nth mode. Separation of variables is achieved by assuming that vertical viscosity is inversely proportional to Brunt-Väisälä frequency [*McCreary*, 1981]. The constant A is chosen so that the damping coefficient for the baroclinic first mode (A/c_1^2) is (12 month)$^{-1}$, which gave the best agreement with observations based on sensitivity experiments conducted by *Nagura and McPhaden* [2010a].

[15] The basin has meridional walls at 40°E and 100°E and is unbounded latitudinally. The reflection of waves at the meridional walls is computed so that summation of zonal velocity due to all meridional modes is zero at the eastern boundary and summation of zonal mass flux is zero at the western boundary [*Clarke*, 1983; *Cane and Gent*, 1984]. A reflection efficiency of 85% in terms of amplitude is assumed on the basis of the observational study of *Le Blanc and Boulanger* [2001]. The analytical method enables us to avoid numerical expedients, such as artificial boundary wave dampers used by *Han et al.* [2001] and *Han* [2005]. The analytical method in our model, on the other hand, is based on specifying boundaries as meridional walls. In reality, the boundaries along the east African coast and Sumatra are slanted, which can cause wave reflections to differ from those at meridional walls [e.g., *Moore and McCreary*, 1990]. However, these differences are negligibly small for waves with zonal scales of O(1000 km) near the equator as demonstrated by *Nagura and McPhaden* [2010a]. *Han et al.* [2011] also demonstrated in a series of linear numerical model simulations that the inclusion of realistic coastlines and the Maldive Islands has relatively little impact on simulated intraseasonal time scale variability near the equator.

[16] In this study we use two versions of the model, as was done by *Nagura and McPhaden* [2010a, 2010b]. The first one, referred to as the "full model," includes fifteen meridional modes (Kelvin mode plus the first fourteen Rossby modes) and the ten gravest baroclinic modes. The second model, which we refer to as "K-R1 model," retains only the two gravest baroclinic mode Kelvin waves and first meridional mode Rossby waves. *Nagura and McPhaden* [2010a, 2010b] found from comparison of the model results with AVISO SSH, OSCAR and moored ADCP measurements that the K-R1 model performs as well as the full model in simulating sea level variability near the equator and is even better than the full model in simulating velocity in the central basin on seasonal to interannual time scales. We confirm these results for intraseasonal time scales in section 4.

[17] For later use, we define how wind stresses are projected onto vertical modes. In the shallow water equations, projected wind forcing is expressed as $\tau^x \psi_n{}^0/(\bar{\rho}H)$, where τ^x denotes zonal wind stress, ψ_n^0 denotes surface value of

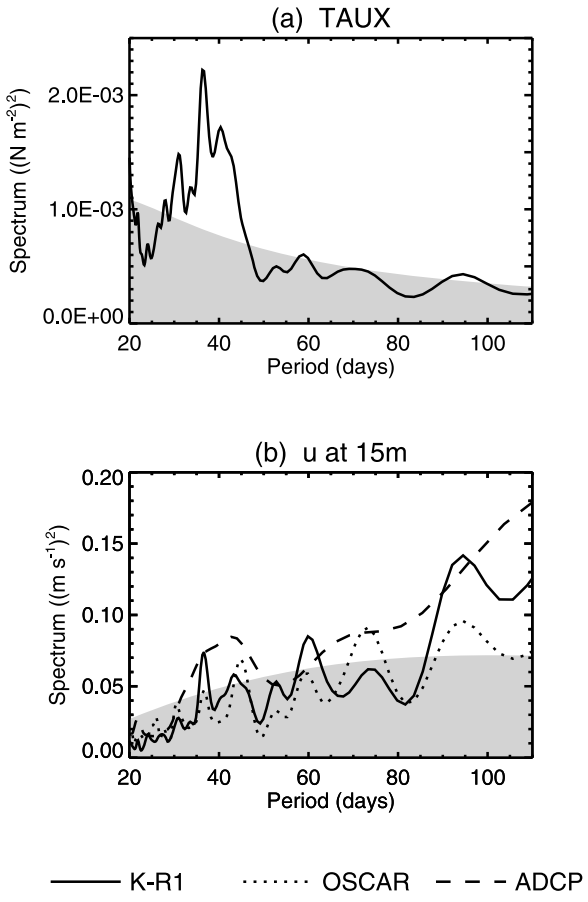

Figure 2. Variance preserving spectra at 0°, 80°E for (a) QSCAT zonal wind stress and (b) zonal velocity at 15 m depth from the K-R1 model (solid line), OSCAR (dotted line), and ADCP observations (dashed line). A triangle filter for three adjacent spectral estimates was applied 10 times to smooth the spectra. The dark shades represent red noise spectra based on a lag-1 autoregressive process [*Gilman et al.*, 1963]. In Figure 2b, the red noise spectrum for model velocity is shown. Those for OSCAR and ADCP velocity are essentially same.

vertical profile of nth baroclinic mode, $\bar{\rho}$ denotes mean seawater density and H is the depth of the ocean floor [see *Nagura and McPhaden*, 2010a, Appendix A]. The velocity scale is expressed in terms of the projected winds as $[\tau^x \psi_n{}^0/(\bar{\rho}H)](\beta c_n)^{-1/2}$ [*Cane*, 1984], where β is meridional gradient of Coriolis parameter and $(\beta\ c_n)^{-1/2}$ is time scale. The specific values of ψ_n^0 and velocity scale are provided by *Nagura and McPhaden* [2010a].

4. Comparison of Observations and Model

[18] As is pointed out in previous studies, zonal wind stress on the equator has its largest power at periods of 30–50 days. The QSCAT wind power spectrum exhibits this 30–50 day peak (Figure 2a) and is relatively flat with minor peaks at longer periods (though the latter are only marginally significant on the basis of the red noise spectrum and not significant according to 90% confidence level of a chi-square distribution). In contrast, the OSCAR surface zonal velocity spectrum is redder, with more power at longer periods. Elevated energy levels at periods of 30–50 days, 60 days, 75 days and 95 days are evident, all of which are statistically significant except for the less energetic peak at 60 days (Figure 2b). This spectrum for zonal velocity is roughly consistent with that for SSH described by *Han et al.* [2001], *Han* [2005], and *Fu* [2007].

[19] The structure of the spectrum from the K-R1 model is remarkably similar to that of OSCAR, albeit with variations in peak energy levels. Most notably, the model tends to be more energetic than OSCAR at periods near 95 days and less energetic near 75 days. The structure of the velocity spectrum for the full model is almost identical to that for the K-R1 model, although energy levels are higher for the full model because more modes are included. The ADCP observations are too short relative to the model and OSCAR to allow for comparable spectral resolution, but the red shift in the mooring spectrum relative to the zonal wind stress spectrum is apparent.

[20] A longitude-period diagram shows that wind variability is vigorous at periods of 30 to 50 days between 60°E to 95°E (Figure 3a). OSCAR velocity has large power to the east of 70°E (Figure 3b) with energy concentrated in the period bands described above. The model velocity spectrum exhibits similar structures though it tends to be more energetic at periods near 60 days and at periods between 90 and 110 days (Figure 3c). OSCAR velocity has some power near the western boundary, but the model misses this variability, probably owing to the lack of nonlinear eddies generated via western boundary current instabilities.

[21] Considering these spectral characteristics together with previous studies that distinguished variability at both high and low frequencies within the intraseasonal band [e.g., *Han et al.*, 2001], we examine the variability at periods of 30–70 days and 70–110 days separately. Variability in the shorter period band is extracted using a Lanczos filter [*Duchon*, 1979] with half power at periods of 30 and 70 days. A Lanczos filter with half power at periods of 70 and 110 days defines variability in the longer period band.

[22] Depth integrated zonal velocity in upper 100 m is compared between the K-R1 model and ADCP observations at 0°, 80.5°E to validate the model results (Figure 4). In both the shorter and longer period bands, the integrated velocity simulated by the K-R1 model compares well with that obtained from ADCP observations. Correlation coefficients are 0.92 for periods of 30–70 days and 0.86 for periods of 70–110 days, both of which are above the 95% significance levels using the degrees of freedom as estimated by *Davis* [1976]. The regression fit (with 95% confidence limits) of the model results to ADCP measurements is indistinguishable from unity at 0.99 ± 0.11 for 30–70 day periods and 1.06 ± 0.23 for 70–110 day periods. Results from the full model are almost identical to those from the K-R1 model, indicating that the two gravest baroclinic modes with Kelvin and first meridional Rossby wave are sufficient to simulate observed intraseasonal variability. Note that intraseasonal variability in OSCAR zonal velocity is also consistent with the model results and ADCP observations at 0°, 80.5°E as expected from discussion of Figures 2 and 3.

[23] The vertical structures of ADCP velocity represented by the first EOF show surface intensified flow and nearly

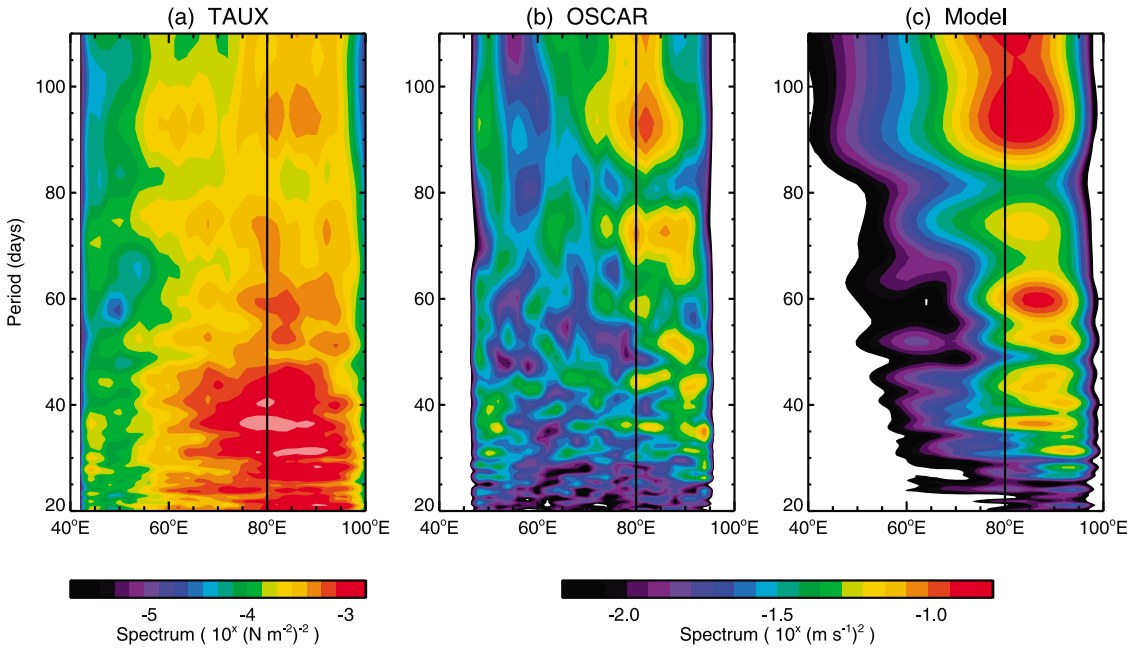

Figure 3. Longitude-period diagram of variance preserving spectra along the equator for (a) QSCAT zonal wind stresses, (b) OSCAR zonal velocity, and (c) K-R1 model surface zonal velocity at 15 m depth.

zero magnitude at about 200 m depth (Figure 5). The first EOFs explain 72% and 71% of total variance at the shorter and longer periods, respectively. The EOF first mode for K-R1 model velocity, which explains 99% of its variance, shows surface intensified vertical profiles similar to the observations, in spite of a slight overestimation in magnitude. Correlations of 0.80 and above between the observations and the K-R1 model first EOF time series are higher than the

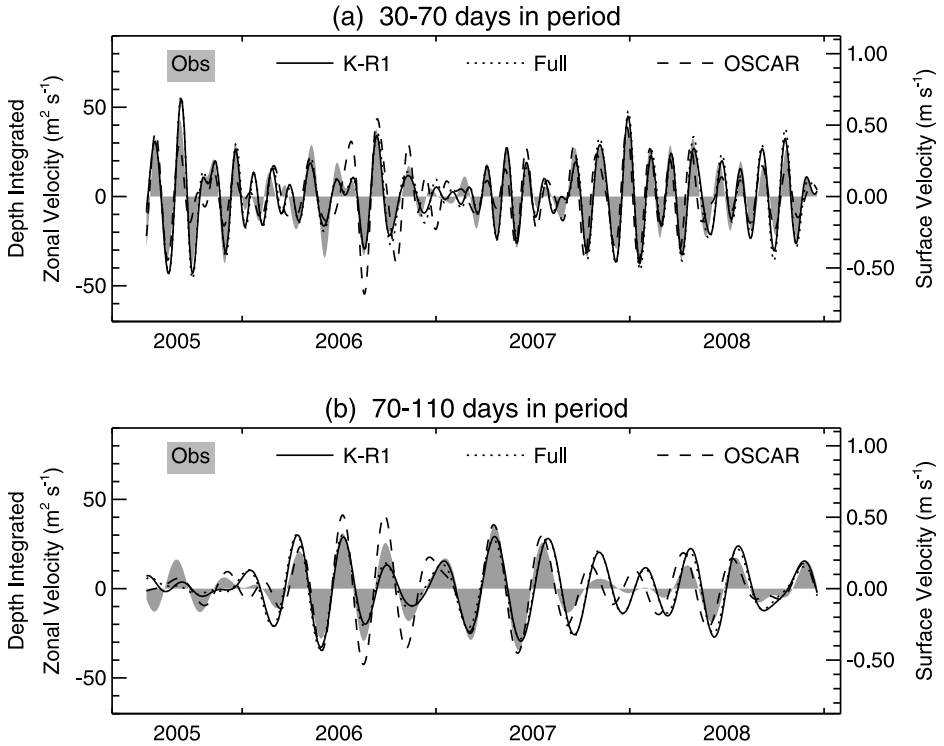

Figure 4. Time series of depth-integrated zonal velocity in upper 100 m at 0°, 80.5°E for ADCP (shading), the K-R1 model (solid line), and the full model (dotted line) for periods of (a) 30–70 days and (b) 70–110 days. The dashed lines show OSCAR zonal velocity at 15 m depth, for which vertical axis is shown on the right.

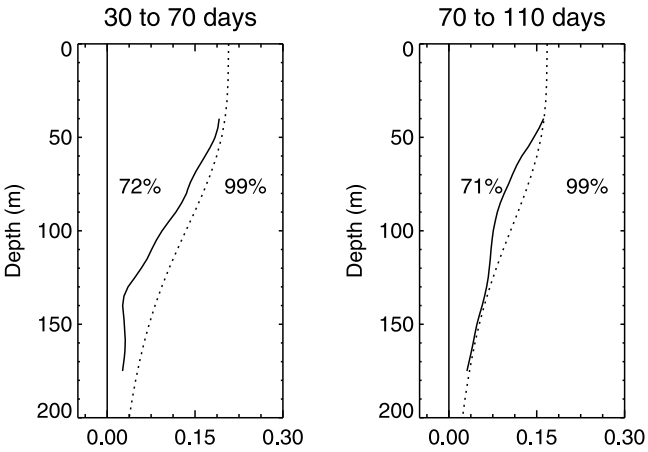

Figure 5. Comparison between ADCP observations (solid lines) and the K-R1 model simulations (dotted lines) at 0°, 80.5°E for vertical profiles of zonal velocity constructed from the first empirical orthogonal function (EOF) for (left) periods of 30–70 days and (right) periods of 70–110 days. The percentages shown are explained variances for velocity with model values on the right and observed values on the left. Correlation coefficients (with the 95% significance levels in the parentheses) between the observations and the model for the first mode time series are 0.88 (0.57) for 30–70 days and 0.80 (0.76) for 70–110 days.

95% significance levels for both period bands, indicating that the model is successful in simulating the basic vertical structure of the observations. Despite differences in detail, our very simple model reproduces observed intraseasonal variations in zonal velocity with enough fidelity to motivate further investigation of the simulations.

5. Effects of Wind Forcing and Equatorial Wave Dynamics on Observed Variability

[24] In this section, we compare observed and simulated variability along the equator, interpreting the results in terms of wind-driven equatorial wave dynamics. Section 5.1 focuses on longitudinal structures in two period bands (30–70 days and 70–110 days), while section 5.2 focuses on processes that lead to reddening of the response spectrum relative to the wind forcing.

5.1. Longitudinal Patterns of Variability

[25] We first compute the pattern of the ocean's response along the equator to intraseasonal zonal wind forcing by regressing velocity and SSH onto a wind index. The index is defined as QSCAT zonal wind stress at 0° 80°E, where intraseasonal winds tend to be strong (Figure 3) [see also *Sengupta et al.*, 2007; *Iskandar and McPhaden*, 2011]. Note that essentially the same results are obtained using wind stresses at slightly different longitudes. The wind index is filtered in period bands of 30–70 days and 70–110 days and normalized by its standard deviation in each period band (Figure 6). The filtered velocity and SSH along the equator are regressed onto the normalized wind index at various time lags. This method helps us to isolate a canonical response to intraseasonal wind forcing along the equator. The resulting regression coefficients for the K-R1 model and OSCAR are shown in Figure 7. One can obtain essentially the same spatial and temporal patterns by applying complex empirical orthogonal function analysis [*Barnett*, 1983] separately to

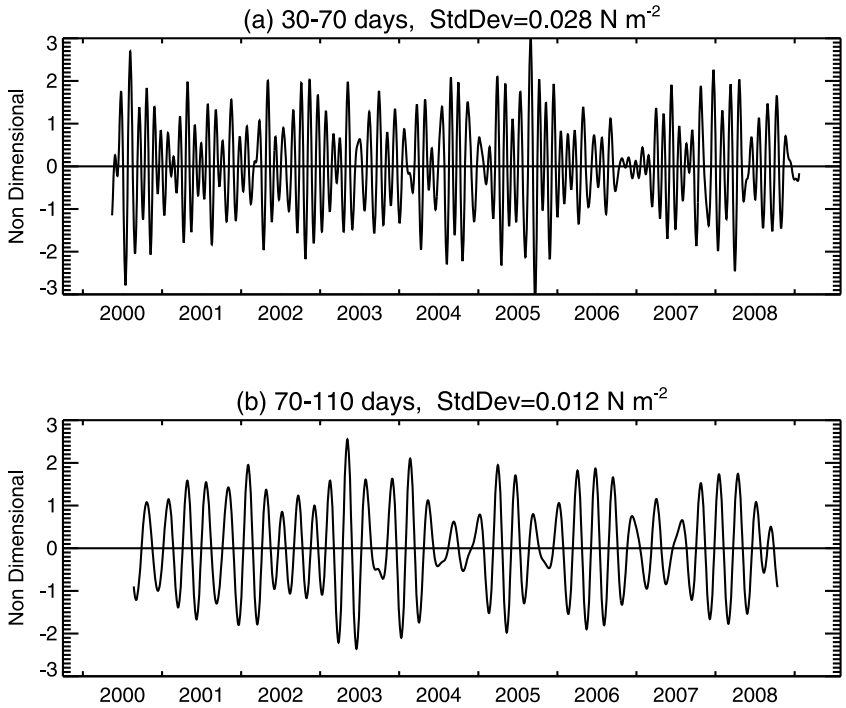

Figure 6. Normalized time series of QSCAT zonal wind stresses at 0°, 80°E at periods of (a) 30–70 days and (b) 70–110 days. The standard deviations used for normalization are shown on top.

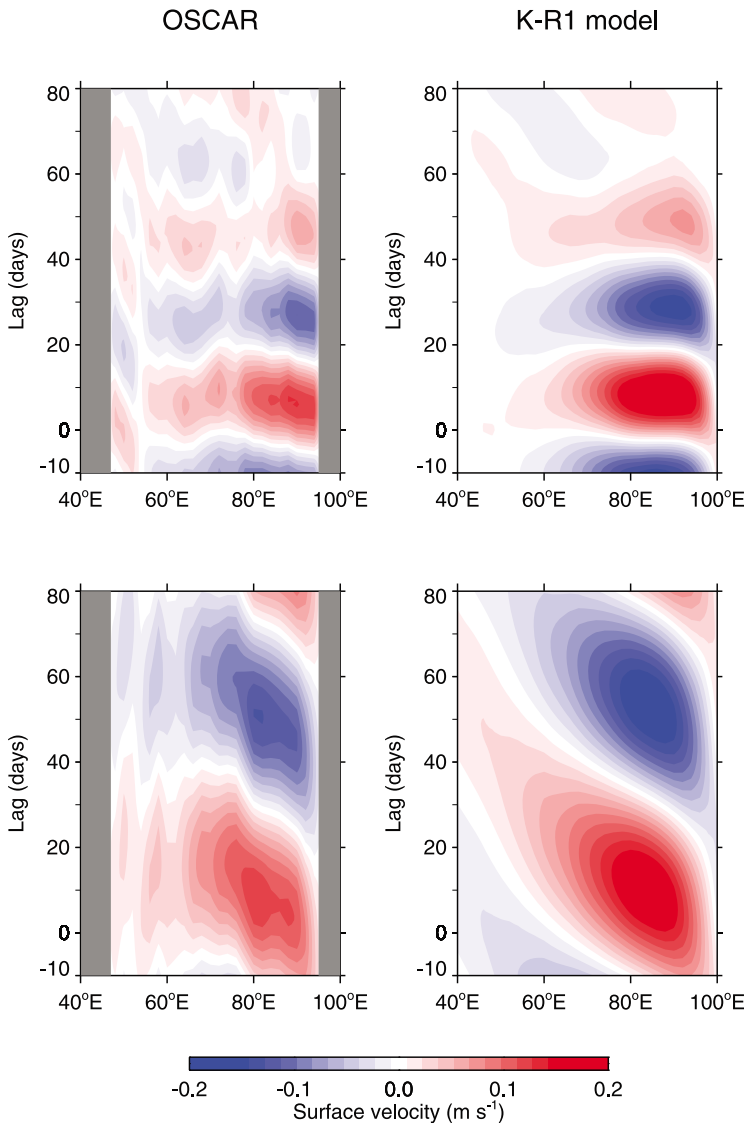

Figure 7. Zonal velocity at 15 m depth along the equator regressed onto the normalized wind index for (left) OSCAR and (right) the K-R1 model. The top regression coefficients are for periods of 30–70 days, and the bottom ones are for periods of 70–110 days.

velocity and winds and then reconstructing the respective leading modes.

[26] OSCAR velocity at 30–70 day periods has its largest magnitude in the eastern basin. It tends to propagate westward east of 70°E and eastward west of 70°E. At 70–110 day periods, OSCAR velocity is strongest east of 60°E with clear tendency of westward propagation. Considering the simplicity of the model, simulated velocity compares remarkably well with OSCAR in both zonal structure and propagation characteristics, except that model velocity at 30–70 day periods tends to be more stationary east of 70°E. This stationarity does not change significantly if we change eastern boundary reflectivity, indicating uncertainty in this model parameter is not the cause of the discrepancy. The model also overestimates amplitude in the eastern half of the basin and does not simulate the small zonal-scale variability in the west. The choice of drag coefficient, tuned for variability across a wide range of intraseasonal to interannual time scales, may account for the amplitude overestimation, while lack of nonlinear eddies in the model probably accounts for the structural discrepancies in the west.

[27] Wind forcing at 30–70 day periods is strong between 60°E to 90°E and oscillates virtually in phase across these longitudes (Figure 8a). The predominant period of this stationary forcing is close to 40 days, which is consistent with the broad spectral peak centered near this period in Figure 2. These winds force Kelvin waves that rapidly propagate eastward and eventually hit the eastern boundary where they reflect into Rossby waves (Figure 8e). The winds also directly force Rossby waves that propagate westward at 1/3 the speed of the Kelvin waves (Figure 8c). The slower zonal phase speed of these waves means that they are attenuated by winds that change sign before the waves completely pass through the forcing region. Thus, unlike the faster forced Kelvin waves, the forced Rossby waves do not reach the western boundary. The net effect is that total velocity tends

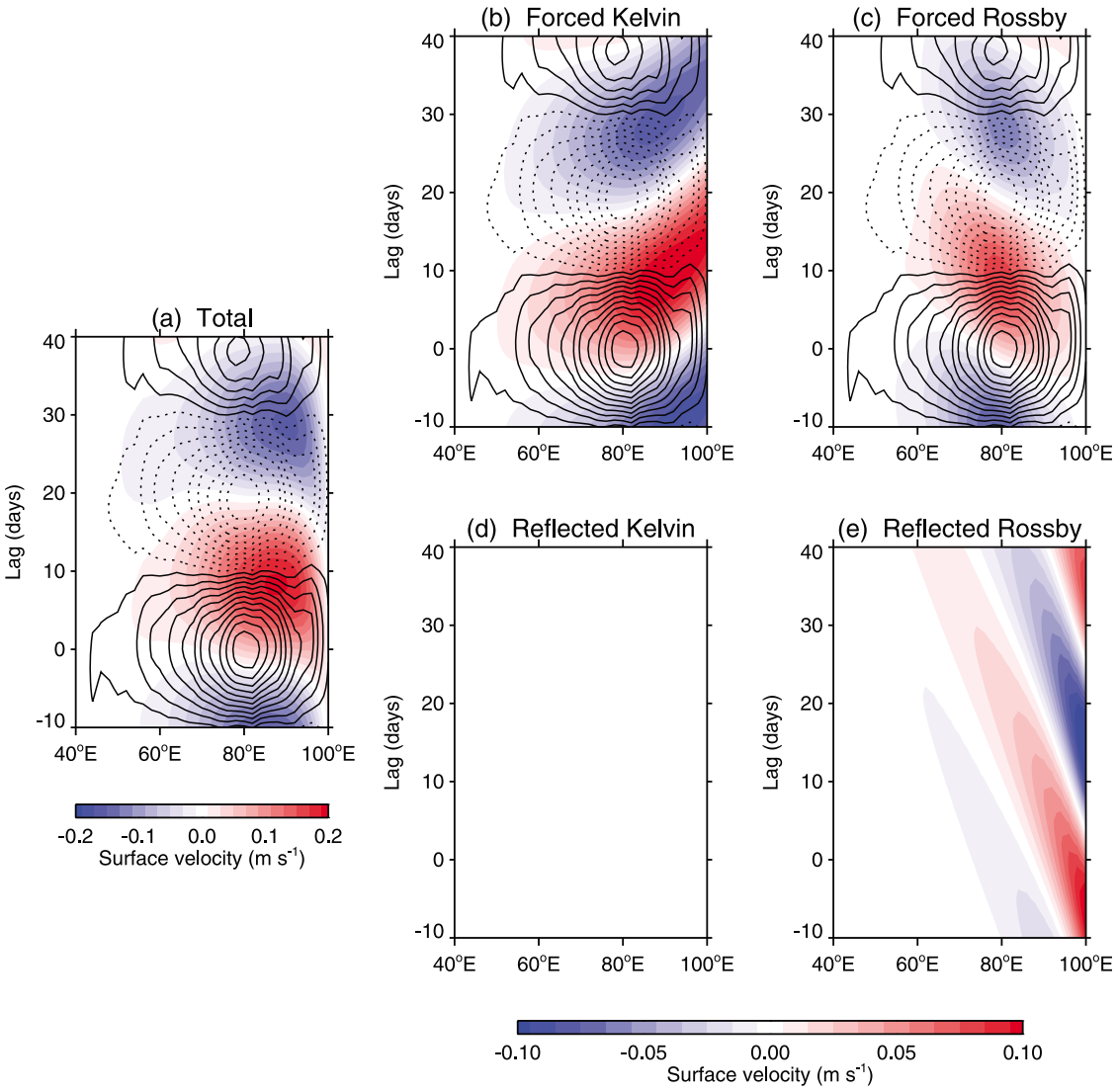

Figure 8. Zonal velocity at 15 m depth along the equator from the K-R1 model regressed onto the normalized wind index at periods of 30–70 days: (a) total solution, (b) forced Kelvin waves, (c) forced Rossby waves, (d) reflected Kelvin waves, and (e) reflected Rossby waves. The contour lines show zonal wind stresses regressed onto the normalized wind index, with eastward winds shown by solid contours and westward winds shown by dotted contours. Contour intervals are 2.5×10^{-3} N m^{-2}, with zero contour omitted. Note that the scale for velocity is different in Figure 8a than in Figures 8b–8e.

to be stationary in the forcing region, with a tendency for eastward propagation to west of about 70°E and westward propagation near the eastern boundary (Figure 8a). Note that phase speed of forced Rossby waves in Figure 8c is faster than that of free, reflected Rossby waves in Figure 8e because of the superposition of the stationary winds on forced waves. *Nagura and McPhaden* [2010a] presented a detailed explanation for how the forcing by stationary winds seemingly boosts wave zonal phase speeds in the forcing region.

[28] The observed SSH in 30–70 day periods has elevated variability in three regions, namely near the western boundary, 60°E–90°E and 90°E–100°E (Figure 9a). The simulated SSH has similar spatial pattern, but misses the variability near the western boundary, probably owing to the lack of nonlinear eddies in the model (Figure 9b). The model SSH associated with forced waves tends to propagate eastward (Figure 9c), indicating dominance of forced Kelvin waves. Westward propagating variations due to reflected Rossby waves are also observed (Figure 9d), but with smaller magnitude compared to the forced Kelvin waves. This is attributable to difference in meridional structure between Kelvin wave and Rossby waves [*Nagura and McPhaden*, 2010a]. The ratio of surface pressure to zonal velocity at the equator (p/u at $y = 0$) is equal to c_n for a Kelvin wave and $c_n/3$ for a Rossby wave. In the case where Kelvin and Rossby wave velocity amplitudes are comparable, the Kelvin wave has larger pressure variability than Rossby wave by a factor of 3. This relationship accounts for the dominance of the

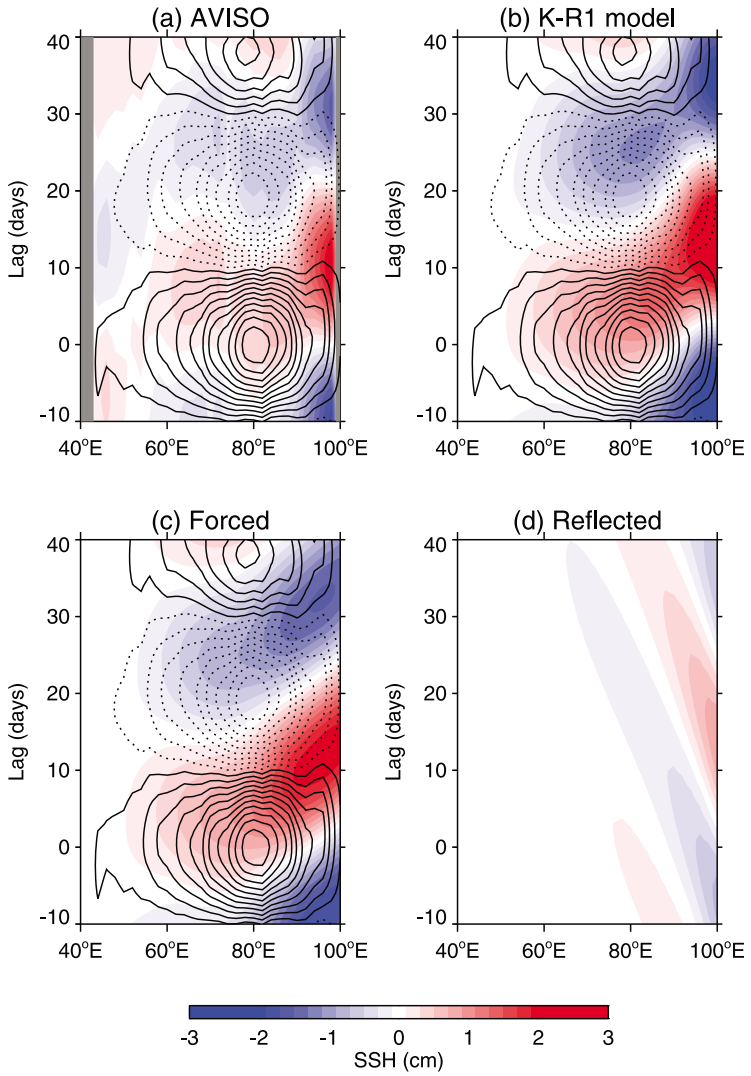

Figure 9. SSH along the equator regressed onto the normalized wind index at periods of 30–70 days for (a) Archiving, Validation, and Interpretation of Satellite Oceanographic data (AVISO) SSH, (b) total K-R1 model SSH, (c) forced K-R1 model SSH, and (d) reflected K-R1 model SSH. Contours are for zonal wind stress as in Figure 8.

Kelvin wave in SSH, which is proportional to pressure in our model.

[29] In contrast to the near-stationary wind forcing at periods of 30–70 days, zonal wind forcing tends to propagate eastward at periods of 70–110 days (Figure 10a). We can estimate the phase speed of the winds via regression fit to a harmonic at each longitude. We chose a period of 90 days, which is in the center of the period band, and longitudinal range of 50°E–100°E, where the eastward propagation is clearly seen. The resultant phase speed estimate is 3.84 $\pm$ 1.77 m s^{-1}, with 95% confidence limits obtained using procedures described by *Emery and Thomson* [2004]. The estimated phase speed for winds is similar in magnitude to the phase speed of the first baroclinic mode Kelvin wave (2.50 m s^{-1}) such that the first mode Kelvin wave is in a near resonant condition [*Hendon et al.*, 1998]. As a result, Kelvin waves are strongly forced in this period band (Figure 10b) and when they reach the eastern boundary they generate reflected Rossby waves with significant amplitude (Figure 10e). The reflected Rossby waves eventually reach the interior ocean and constructively interfere with forced waves. For example, westward velocity due to reflected Rossby waves overlaps that due to forced Kelvin waves in 60°E–80°E around day +60. Wind forcing also excites Rossby waves in the interior ocean, which are attenuated by winds of opposite sign between 50°–80°E (Figure 10c). Consequently, forced Rossby waves do not reach the western boundary with sufficiently large amplitude to generate reflected Kelvin waves (Figure 10d). The net effect of these wave processes is that while the winds propagate eastward along the equator, zonal velocity propagates westward because of the combined influence of forced and eastern boundary generated Rossby waves (Figure 10a).

[30] Observed SSH variability at 70–110 day periods forms an east-west pattern with a node at about 85°E such that SSH tends to be out of phase between 60°E–85°E and

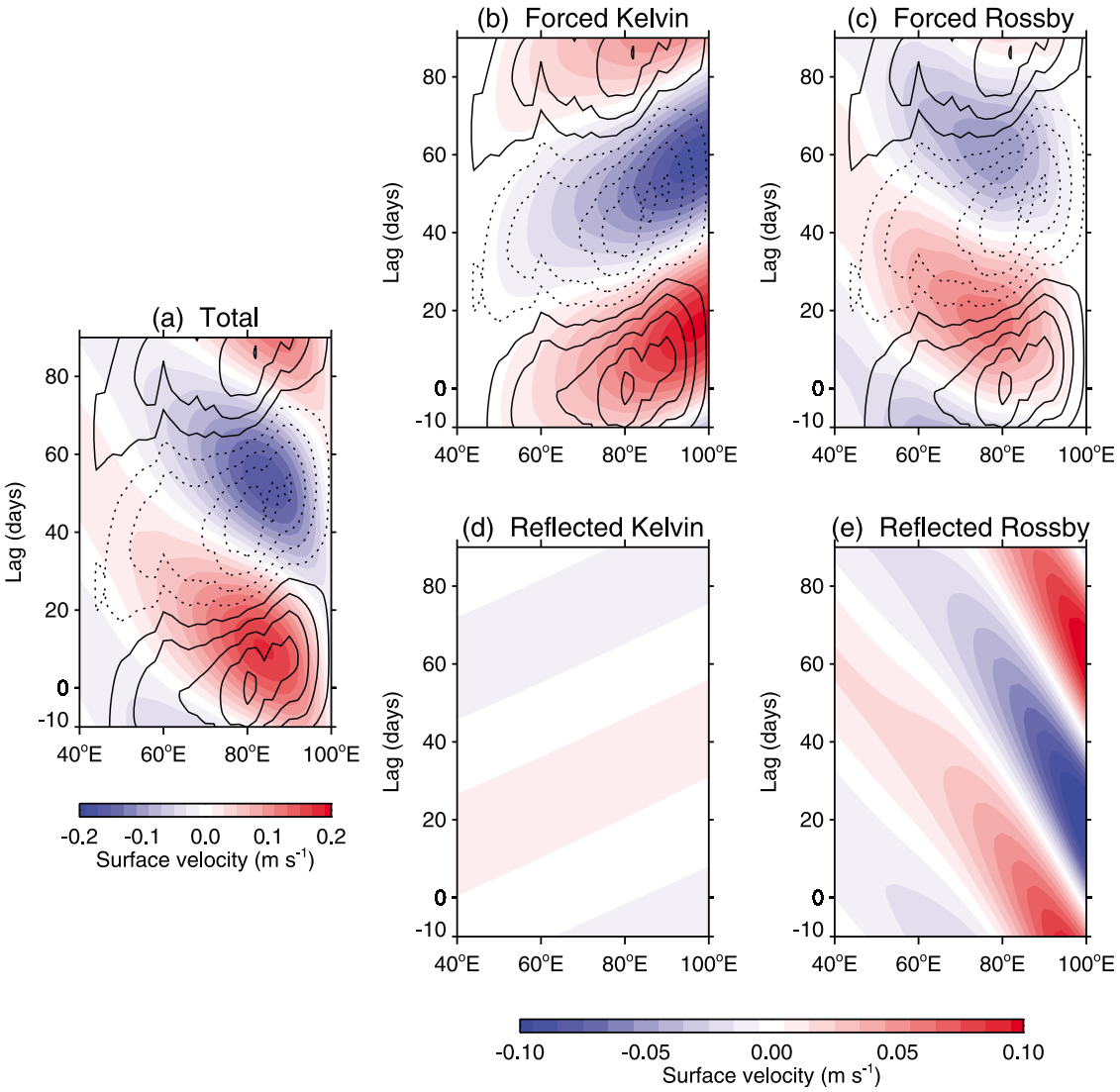

Figure 10. (a–e) Same as Figure 8 but for periods of 70–110 days.

85°E–100°E (Figure 11a). The simulated SSH has a similar spatial pattern with similar magnitude, although the node is less sharply defined (Figure 11b). Forced SSH tends to propagate eastward under the influence of Kelvin wave dynamics (Figure 11c), while eastern boundary generated SSH (Figure 11d) propagates westward in the form of Rossby waves. SSH appears to propagate westward near the western boundary because of the superposition of Rossby waves arriving from the east on weaker western boundary generated Kelvin waves.

[31] The K-R1 model has two baroclinic modes, which are comparable in magnitude for zonal velocity at 30–70 day periods (Figure 12a). The first baroclinic mode Kelvin wave can cross the forcing region in 15 days and at a fixed frequency has a longer zonal wavelength than the second baroclinic mode, which takes 25 days to traverse the forcing region. For zonally stationary winds, one might expect that faster and longer-wavelength first baroclinic mode waves (which are also less strongly damped than second baroclinic mode waves) would be preferentially excited. However, the wind stress preferentially projects onto the second mode in our model, as determined using a velocity scale that is roughly proportional to $c_n^{-1/2}$ (see section 3). Thus, the two vertical modes end up having similar magnitudes at 30–70 day periods.

[32] *Han et al.* [2001, 2011], *Han* [2005], and *Fu* [2007] argued that the second baroclinic mode dominates at about 90 day periods since second baroclinic mode wave phase speeds favor a basin mode resonance. Our results show that the first mode is larger west of 80°E while the second mode is dominant to the east for the period band of 70–110 days that encompasses the 90 day peak (Figure 12b). According to *Cane and Moore* [1981], the velocity for the first and second modes would have an expected maximum amplitude at about 78°E and 86°E, respectively, at 90 day periods due to constructive interference between Kelvin waves and eastern boundary generated Rossby waves (Appendix A). These theoretical estimates compare well with our results in Figure 12b. In addition, with realistic zonal wind stress forcing that propagates eastward at these periods, the first

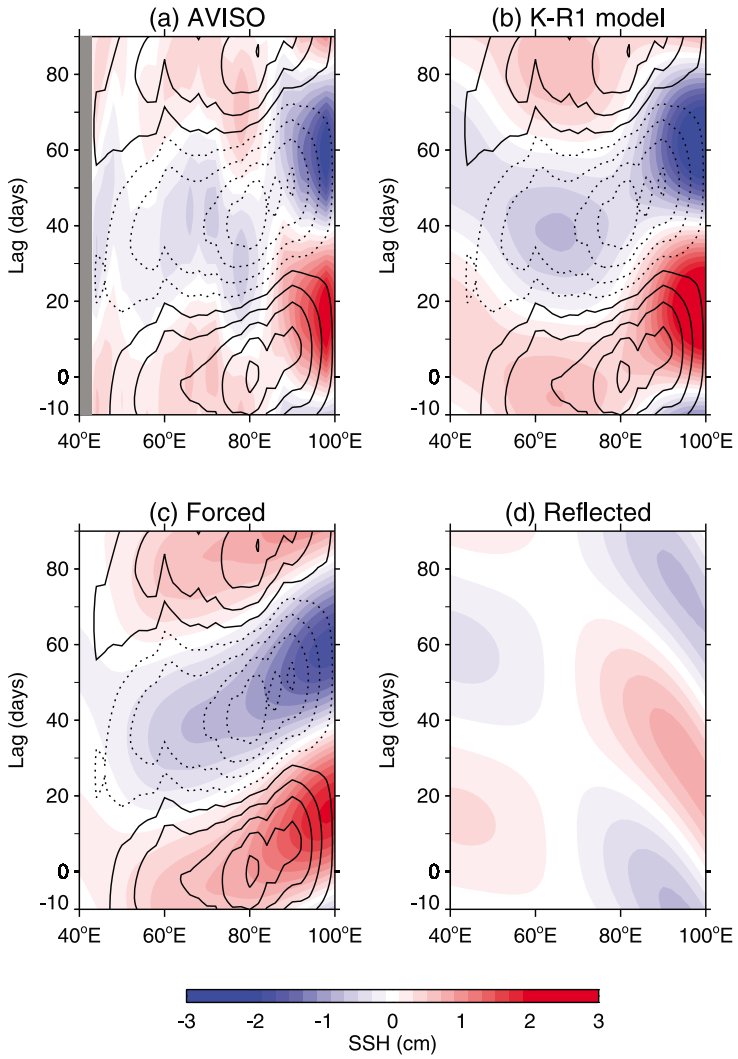

Figure 11. (a–d) Same as Figure 9 but for periods of 70–110 days.

baroclinic mode Kelvin wave is strongly excited; it has a broader zonal extent than the second baroclinic mode, with a maximum amplitude near 80°E where the regressed forcing is strongest (Figure 10). It is noteworthy that we do not see a local secondary amplitude maximum in the western basin near 55°E for the second baroclinic mode as in *Han et al.*'s [2011] model results, which they considered as indicative of a basin mode resonance.

5.2. Spectral Characteristics

[33] As mentioned earlier, velocity spectra are red relative to the forcing spectrum, which has its peak energy at 30–50 days (Figure 2). This reddening is in part due to the mechanism proposed by *Kessler et al.* [1995] for intraseasonal variability in the equatorial Pacific Ocean. Specifically, low-frequency nondispersive Kelvin and Rossby waves will be preferentially excited because the lower-frequency waves have longer zonal wavelengths compared to the wind fetch. Shorter-period, shorter-wavelength waves in contrast will be less strongly excited because of wind work done against these waves as they traverse the forcing region. At periods between 70 and 110 days, additional factors contribute to boosting zonal velocity energy levels (Figure 2). The near resonant forcing by eastward propagating winds (Figure 10) generates significant near 90 day variability in velocity (Figure 13b) with a substantial contribution from the first baroclinic mode (Figure 13c). The power in forced zonal velocity at near 90 day periods is comparable to that at 30–70 day periods, while total velocity variability is twice as large as 30–70 day periods (Figure 13a). This difference is due to the importance of reflected Rossby waves (Figure 13b), which have considerable energy at periods longer than 80 days and contribute to constructive interference with forced waves as discussed in section 5.1. Note however that peaks in the forced only Rossby and Kelvin waves indicate that a peak in total variance at this period would arise even without considering boundary generated Rossby waves possibly because wind forcing, though relatively weak at these periods, has marginally significant energy peak at about 90 day periods.

[34] As Figures 8, 10, and 13b show, Rossby waves dominate the reflected wavefield and Kelvin waves reflected from the western boundary are negligible on intraseasonal time scales in the Indian Ocean. This result is not consistent with the existence of basin mode resonances, which *Han et al.* [2001, 2011] and *Han* [2005] proposed as a mechanism for

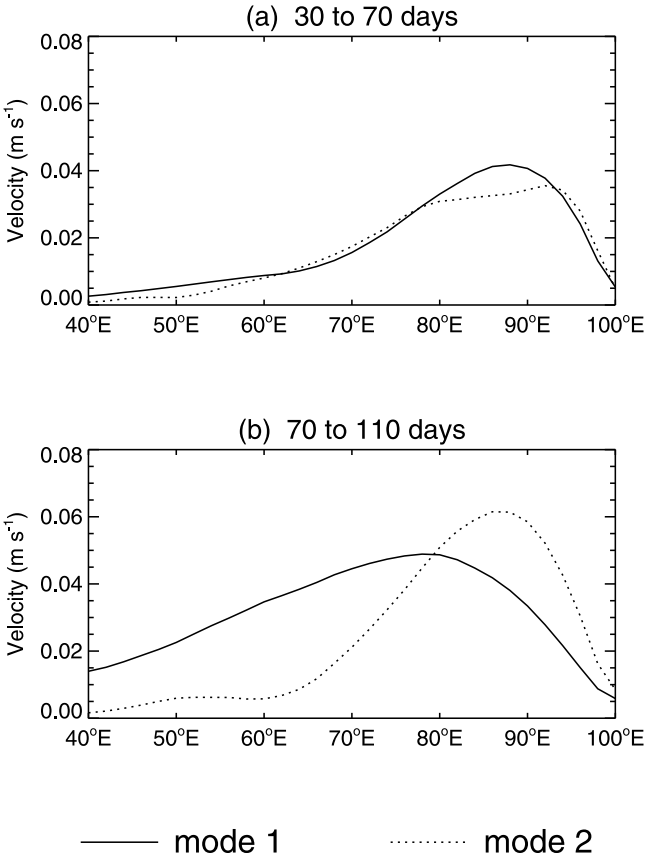

Figure 12. Standard deviations of the first (solid lines) and second (dotted lines) baroclinic modes regressed onto the wind index for zonal velocity at 15 m depth along the equator in the (a) 30–70 day period band and (b) 70–110 day period band.

the excitation of intraseasonal variability at 90 day periods. To explore this issue in more detail, we perform additional experiments in which either of eastern or western boundary reflectivity is changed from 0% to 100%. If eastern boundary reflection is eliminated, velocity energy levels are reduced by about a third at 55–85 day periods and more than halved at 90 day periods (Figure 14a). The reduction of the western boundary reflection has much less impact on velocity energy levels (Figure 14b).

[35] These results indicate that the eastern boundary reflected Rossby waves are essential for an accurate understanding of intraseasonal variability in the 70–110 day period band, in addition to near resonant forcing by the eastward propagating winds. Basin modes, which include both reflected Kelvin and Rossby waves, are not found in our model solutions. This conclusion contradicts the results obtained by *Han et al.* [2011], who found that the 90 day peak in velocity spectrum simulated by a conceptual one-dimensional model vanishes if western boundary reflection is eliminated. We surmise that this difference is due to differences in the models used. The conceptual model *Han et al.* [2011] used ignores energy loss at the western boundary due to excitation of short Rossby waves, and thus possibly exaggerates western boundary generated waves. Our model is more realistic to the extent that the energy loss at the boundaries is taken into account by the long-wave approximation.

6. Summary and Discussion

[36] In this study a simple analytical linear long-wave model is used to investigate intraseasonal variability along the equator in the Indian Ocean. The model is forced by QSCAT satellite winds and is highly simplified, with a flat bottom, meridional walls for eastern and western boundaries, and just the two gravest baroclinic mode Kelvin waves and first meridional mode Rossby waves. Despite of the extreme simplicity of the model however, simulated velocity and SSH compare well with in situ and satellite observations in terms of horizontal structure, vertical structure and spectral content. As noted in past studies, the observed and modeled velocity spectra are much redder compared to the wind forcing.

[37] At periods of 30–70 days, zonal wind forcing is on average stationary in longitude. We might have expected eastward propagation of the winds as at periods of 70–110 days because of the influence of the Madden Julian Oscillation (MJO), which extends over the periods of approximately 30–100 days [*Zhang*, 2005]. One possible reason for this unexpected behavior is that the MJO accounts for only about 50% of the variance at intraseasonal time scales [e.g., *Kessler*, 2001] and there are other sources of atmospheric variability in this period band. Examination of the wind stress time series indicates periods of eastward propagation as well as periods of no or even westward propagation.

[38] Regardless of why the surface zonal winds at 30–70 day periods are on average stationary in longitude over the period of our study, they preferentially excite Kelvin waves whose zonal wavelengths are long compared to the fetch of the wind. For nondispersive Kelvin waves, the selection mechanism favors lower-frequency Kelvin waves over higher-frequency, shorter-wavelength Kelvin waves. Rossby waves, which propagate westward at phase speeds much slower than eastward propagating Kelvin waves, are attenuated by the winds before completely passing through the forcing region. However, the contribution from Rossby waves is still sizable, so that total velocity tends to be stationary in the forcing region owing to the combined influence of Kelvin and Rossby waves. Both first and second baroclinic modes make comparable contributions to surface zonal velocity variations. Faster phase speeds and weaker damping favor excitation of the first baroclinic mode. On the other hand, winds project more efficiently onto the second mode, so that the two vertical modes end up having similar magnitudes.

[39] At periods of 70–110 days, wind forcing tends to migrate eastward, resonantly forcing Kelvin waves. The forced Kelvin waves hit the eastern boundary and generate reflected Rossby waves with substantial amplitude, constructively interfering with the directly wind forced waves in the interior ocean. This constructive interference boosts energy especially at periods around 90 days. The net effect of these wave processes is that while the wind forcing propagates eastward along the equator, zonal velocity propagates westward.

[40] Previous studies emphasized the importance of basin mode resonances, in which both eastern boundary generated waves and western boundary generated waves are essential,

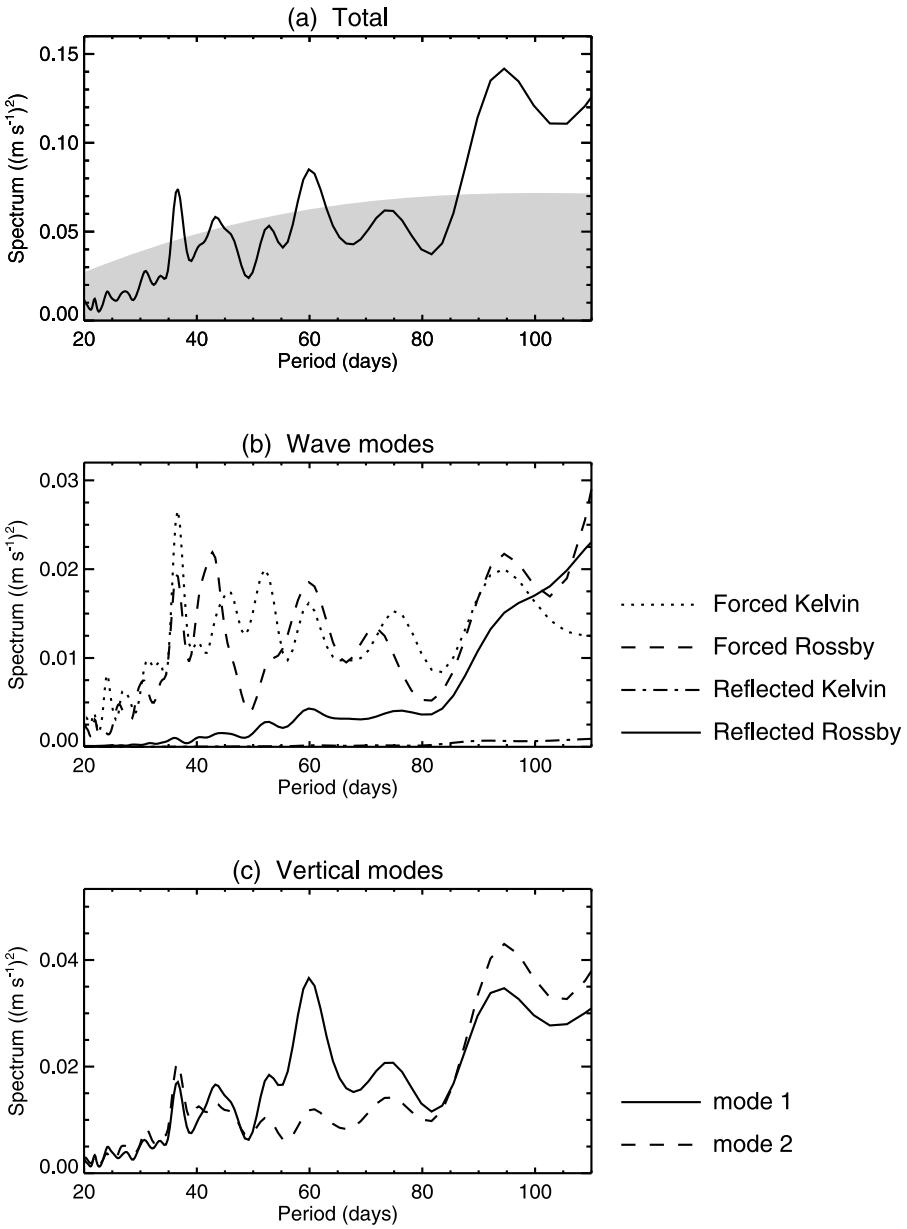

Figure 13. Variance preserving spectra for 15 m zonal velocity at 0°, 80°E from the K-R1 model: (a) total velocity, (b) forced Kelvin waves (dotted line), forced Rossby waves (dashed line), reflected Kelvin waves (dash-dotted line), and reflected Rossby waves (solid line), and (c) the first baroclinic mode (solid line) and the second baroclinic mode (dashed line). The shading shown in Figure 13a represents red noise spectra based on a lag-1 autoregressive process [*Gilman et al.*, 1963].

in the excitation of intraseasonal variability in the Indian Ocean [*Han et al.*, 2001, 2011; *Han*, 2005; *Fu*, 2007]. Our experiments in which boundary reflectivity is artificially reduced to zero show that zonal velocity energy levels hardly change if western boundary reflection is eliminated. On the other hand, we find that eastern boundary reflectivity has a crucial impact on zonal velocity energy levels. These results suggest that constructive interference between wind forced waves in the interior ocean and Rossby waves reflected from eastern boundary, rather than basin mode dynamics, are essential in generating observed variability. Consistently, our model results also do not show double maxima in amplitude along the equator for second baroclinic mode velocity at periods near 90 days, which *Han et al.* [2011] found in idealized wind-driven experiments and which they invoked as evidence for basin mode resonance.

[41] Our results may help to reconcile the apparent discrepancy between the 180 day adjustment time in idealized transient model simulations highlighted by *Han et al.* [2011] and *Sengupta et al.*'s [2007] assertion, also from idealized transient model experiments, that 80–100 days is an intrinsic time scale for equatorial Indian Ocean adjustment. *Han et al.* [2001] defined the adjustment time scale on the basis of baroclinic second mode wave speeds, while *Sengupta et al.* [2007] measured the time scale using depth integrated zonal pressure gradient, which emphasized the first baroclinic mode

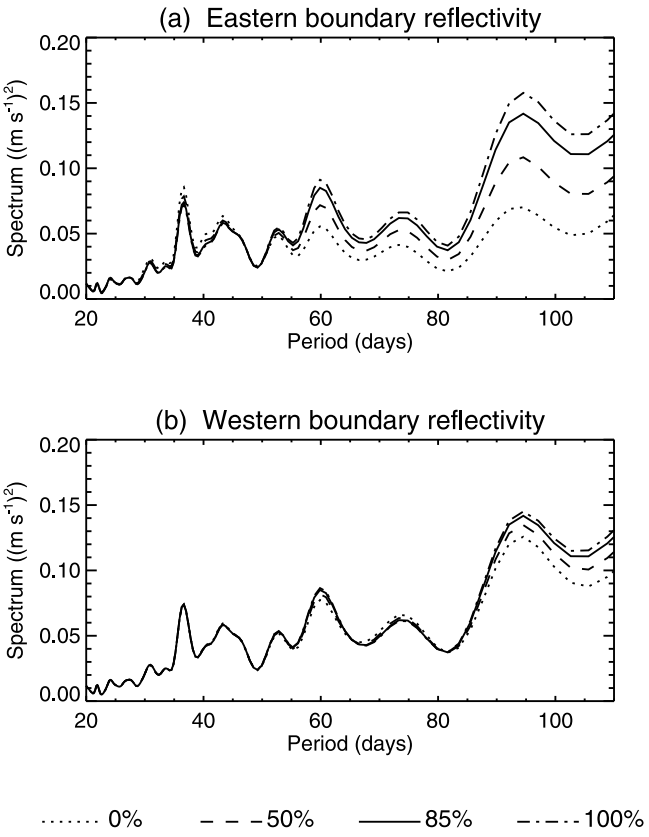

Figure 14. (a) Spectra at 0°, 80°E for the K-R1 model zonal velocity at 15 m depth from the experiments in which the eastern boundary reflectivity is changed from 0% to 100%. The western boundary reflectivity is kept as the standard value (85%). (b) Same as Figure 14a but for the experiments with various western boundary reflectivity and constant eastern boundary reflectivity (85%).

in the initial phases of the ocean's adjustment. Both modes are strongly evident in our model results forced by realistic winds and, by extension, in observed variability that is so well represented by our model.

[42] In summary, our results suggest that the red shift in the velocity spectrum relative to the wind forcing spectrum is attributable to a combination of factors. These include (1) the near resonant excitation of Kelvin waves by eastward propagating winds, (2) the constructive interference between wind-forced waves and Rossby waves reflected from the eastern boundary, and (3) the favored excitation of waves whose zonal wavelengths are long compared to the fetch of the wind. For nondispersive Kelvin and Rossby waves, this latter mechanism favors lower frequencies over higher frequencies in the intraseasonal band. The first two of these mechanisms are particularly pronounced at periods of 70–110 days and contribute significantly to the energy peak near 90 days. These results help to define more precisely the dynamics of wind-driven intraseasonal variability in the equatorial Indian Ocean. It is known that intraseasonal variations on the equator can affect coastal currents along the western coast of the Indian Peninsula [*Vialard et al.*, 2009] and also lower frequencies associated with the seasonal Wyrtki Jets and interannual Indian Ocean Dipole [e.g., *Han et al.*, 2004; *Masumoto et al.*, 2005]. Thus, a better understanding of this intraseasonal variability constitutes an important step forward in developing a comprehensive theory of climate variability in the region.

Appendix A: Constructive Interference of Kelvin and Reflected Rossby Waves

[43] This appendix summarizes the mathematical formulation of *Cane and Moore* [1981] for the constructive interference of Kelvin and Rossby waves as it applies to our study. They solved the linear, inviscid, nondimensionalized shallow water equations on the equatorial β-plane given by

$$\begin{cases} u_t - yv + h_x = 0, & \text{(A1a)} \\ v_t + yu + h_y = 0, & \text{(A1b)} \\ h_t + u_x + v_y = 0. & \text{(A1c)} \end{cases}$$

From equations (A1a)–(A1c), they obtained an analytical solution for velocity from the summation of Kelvin wave and reflected Rossby wave modes:

$$u = 2^{\frac{1}{2}}\pi^{\frac{1}{4}}e^{i\omega t}\left\{\psi_0 e^{-is} + \sum_{l=1}^{\infty}\alpha_1^l\left((l+1)^{-\frac{1}{2}}\psi_{l+1} - l^{-\frac{1}{2}}\psi_{l-1}\right)e^{i(2l+1)s}\right\}, \quad \text{(A2)}$$

where ω is scaled frequency, s is a zonal coordinate ($s = \omega(x–X_E)$, x is scaled longitude, X_E is the scaled longitude of the eastern boundary), l is meridional mode number, and ψ_l is lth Hermite function. The first term in the curly bracket is the Kelvin wave mode and the second term represents reflected Rossby wave modes. The Rossby wave coefficient α_1^l is chosen so that zonal velocity is zero at the eastern boundary, which is assumed to be a perfectly reflecting meridional wall. The summation is only over odd numbered modes (l = 1, 3, 5...) for a straight north-south boundary, because Kelvin waves do not project onto even numbered meridional mode Rossby waves. Using the long-wave approximation, the infinite sum in the above equation can be written as a simple formula:

$$u = -i\tan 2s(\cos 2s)^{\frac{1}{2}}\exp i\left[\frac{y^2}{2}\tan 2s\right]e^{i\omega t}. \quad \text{(A3)}$$

The consequence of this expression in a theoretical sense is that there are singularities or "caustics" at focal points where the velocity amplitude is very large. The focal point is defined as the longitude where cos(2s) = 0 and is caused by constructive interference between Kelvin and reflected Rossby waves. When the number of meridional Rossby modes is truncated to less than infinity, when friction is added, or when there is an irregular coast line, the waves are defocused and the singularities become regions where constructive interference results in large amplitude. These solutions are free wave solutions but the dynamics should apply in the case of wind forcing.

[44] The longitude of the focal points can be computed using cos(2s) = 0, or $2\omega(x - X_E) = (2m + 1)\pi/2$ (m is a negative integer). In dimensional form, the focal point is at $X_E^* + (2m + 1)\pi/(4\omega^*)$, where X_E^* denotes dimensional

longitude of the eastern boundary and ω^* is dimensional frequency. There are multiple focal points corresponding to different m's. As m decreases, the focal point becomes farther from the eastern boundary; waves need to travel for longer distance and are weakened more owing to damping. Thus the clearest focal point is the one closest to the eastern boundary ($m = -1$), which is 78°E for the first baroclinic mode and 86°E for the second mode at 90 day periods, for $X_E^* = 100$°E.

[45] The basin mode referred to by *Han et al.* [2001, 2011] and *Han* [2005] is the special case of the solution (A3). If the western boundary condition is added, $\int_{-\infty}^{\infty} u dy = 0$ must be satisfied zero at $x = 0$. This condition requires $\sin(-\omega X_E) = 0$, or $-2\omega X_E = n\pi$ (n is a positive integer). Rewriting $\omega = 2\pi/P$, where P is the scaled period, $P = 4X_E/n$. In dimensional form, it is $P = 4X_E^*/(nc)$, where c denotes phase speed of Kelvin wave. *Han et al.* [2001, 2011] and *Han* [2005] used this equation to compute periods of basin mode resonance.

[46] **Acknowledgments.** The authors thank Dennis Moore for his valuable insights on the theory of equatorial wave dynamics. The authors would like to acknowledge the insightful comments from two anonymous reviewers as well. We thank the Coriolis Data Center for providing the gridded temperature and salinity data set; Remote Sensing Systems for providing QSCAT data; the Ssalto/Duacs (Developing Use of Altimetry for Climate Studies) project for the gridded SSH data; and Earth and Space Research for OSCAR velocity analysis. NOAA's Climate Program Office supported production of this manuscript. This is PMEL contribution 3599.

References

Barnett, T. P. (1983), Interaction of the monsoon and Pacific trade wind system at interannual time scales. Part I: The equatorial zone, *Mon. Weather Rev.*, *111*, 756–773, doi:10.1175/1520-0493(1983)111<0756:IOTMAP>2.0.CO;2.

Bonjean, F., and G. S. E. Lagerloef (2002), Diagnostic model and analysis of the surface currents in the tropical Pacific Ocean, *J. Phys. Oceanogr.*, *32*, 2938–2954, doi:10.1175/1520-0485(2002)032<2938:DMAAOT>2.0.CO;2.

Brandt, P., M. Dengler, A. Rubino, D. Quadfasel, and R. Schott (2003), Intraseasonal variability in the southwestern Arabian Sea and its relation to the seasonal circulation, *Deep Sea Res., Part II*, *50*, 2129–2141.

Cane, M. A. (1984), Modeling sea level during El Niño, *J. Phys. Oceanogr.*, *14*, 1864–1874, doi:10.1175/1520-0485(1984)014<1864:MSLDEN>2.0.CO;2.

Cane, M. A., and P. R. Gent (1984), Reflection of low-frequency equatorial waves at arbitrary western boundaries, *J. Mar. Res.*, *42*, 487–502, doi:10.1357/002224084788505988.

Cane, M. A., and D. W. Moore (1981), A note on low-frequency equatorial basin modes, *J. Phys. Oceanogr.*, *11*, 1578–1584, doi:10.1175/1520-0485(1981)011<1578:ANOLFE>2.0.CO;2.

Clarke, A. J. (1983), The reflection of equatorial waves from oceanic boundaries, *J. Phys. Oceanogr.*, *13*, 1193–1207, doi:10.1175/1520-0485(1983)013<1193:TROEWF>2.0.CO;2.

Clarke, A. J., and X. Liu (1993), Observations and dynamics of semiannual and annual sea levels near the eastern equatorial Indian Ocean boundary, *J. Phys. Oceanogr.*, *23*, 386–399, doi:10.1175/1520-0485(1993)023<0386:OADOSA>2.0.CO;2.

Davis, R. E. (1976), Predictability of sea surface temperature and sea level pressure anomalies over the North Pacific Ocean, *J. Phys. Oceanogr.*, *6*, 249–266, doi:10.1175/1520-0485(1976)006<0249:POSSTA>2.0.CO;2.

Ducet, N., P. Y. Le Traon, and G. Reverdin (2000), Global high resolution mapping of ocean circulation from TOPEX/POSEIDON and ERS 1 and 2, *J. Geophys. Res.*, *105*, 19,477–19,498, doi:10.1029/2000JC900063.

Duchon, C. E. (1979), Lanczos filtering in one and two dimensions, *J. Appl. Meteorol.*, *18*, 1016–1022, doi:10.1175/1520-0450(1979)018<1016:LFIOAT>2.0.CO;2.

Emery, W. J., and R. E. Thomson (2004), *Data Analysis Methods in Physical Oceanography*, Elsevier, Amsterdam.

Foltz, G. R., and M. J. McPhaden (2010a), Interaction between the Atlantic meridional and Niño modes, *Geophys. Res. Lett.*, *37*, L18604, doi:10.1029/2010GL044001.

Foltz, G. R., and M. J. McPhaden (2010b), Abrupt equatorial wave-induced cooling of the Atlantic cold tongue in 2009, *Geophys. Res. Lett.*, *37*, L24605, doi:10.1029/2010GL045522.

Fu, L.-L. (2007), Intraseasonal variability of the equatorial Indian Ocean observed from sea surface height, wind and temperature data, *J. Phys. Oceanogr.*, *37*, 188–202, doi:10.1175/JPO3006.1.

Gilman, D. L., F. J. Fuglister, and J. M. Mitchell Jr. (1963), On the power spectrum of "red noise," *J. Atmos. Sci.*, *20*, 182–184, doi:10.1175/1520-0469(1963)020<0182:OTPSON>2.0.CO;2.

Han, W. (2005), Origins and dynamics of the 90-day and 30–60-day variations in the equatorial Indian Ocean, *J. Phys. Oceanogr.*, *35*, 708–728, doi:10.1175/JPO2725.1.

Han, W., D. M. Lawrence, and P. J. Webster (2001), Dynamical response of equatorial Indian Ocean to intraseasonal winds: Zonal flow, *Geophys. Res. Lett.*, *28*(22), 4215–4218, doi:10.1029/2001GL013701.

Han, W., P. Webster, R. Lukas, P. Hacker, and A. Hu (2004), Impact of atmospheric intraseasonal variability in the Indian Ocean: Low-frequency rectification in equatorial surface current and transport, *J. Phys. Oceanogr.*, *34*, 1350–1372, doi:10.1175/1520-0485(2004)034<1350:IOAIVI>2.0.CO;2.

Han, W., J. P. McCreary, Y. Masumoto, J. Vialard, and B. Duncan (2011), Basin resonances in the equatorial Indian Ocean, *J. Phys. Oceanogr.*, *41*, 1252–1270, doi:10.1175/2011JPO4591.1.

Hendon, H. H., B. Liebmann, and J. D. Glick (1998), Oceanic Kelvin waves and the Madden-Julian Oscillation, *J. Atmos. Sci.*, *55*, 88–101, doi:10.1175/1520-0469(1998)055<0088:OKWATM>2.0.CO;2.

Iskandar, I., and M. J. McPhaden (2011), Dynamics of wind-forced intraseasonal zonal current variations in the equatorial Indian Ocean, *J. Geophys. Res.*, *116*, C06019, doi:10.1029/2010JC006864.

Kessler, W. S. (2001), EOF representations of the Madden-Julian Oscillation and its connection with ENSO, *J. Clim.*, *14*, 3055–3061, doi:10.1175/1520-0442(2001)014<3055:EROTMJ>2.0.CO;2.

Kessler, W. S., M. J. McPhaden, and K. M. Weickmann (1995), Forcing of intraseasonal Kelvin waves in the equatorial Pacific Ocean, *J. Geophys. Res.*, *100*, 10,613–10,631, doi:10.1029/95JC00382.

Le Blanc, J.-L., and J.-P. Boulanger (2001), Propagation and reflection of long equatorial waves in the Indian Ocean from TOPEX/POSEIDON data during the 1993–1998 period, *Clim. Dyn.*, *17*, 547–557, doi:10.1007/s003820000128.

Luyten, J. R., and D. H. Roemmich (1982), Equatorial currents at semiannual period in the Indian Ocean, *J. Phys. Oceanogr.*, *12*, 406–413, doi:10.1175/1520-0485(1982)012<0406:ECASAP>2.0.CO;2.

Masumoto, Y., H. Hase, Y. Kuroda, H. Matsuura, and K. Takeuchi (2005), Intraseasonal variability in the upper layer currents observed in the eastern equatorial Indian Ocean, *Geophys. Res. Lett.*, *32*, L02607, doi:10.1029/2004GL021896.

McCreary, J. (1981), A linear stratified ocean model of the equatorial undercurrent, *Philos. Trans. R. Soc. London A*, *298*, 603–635, doi:10.1098/rsta.1981.0002.

McPhaden, M. J. (1982), Variability in the central equatorial Indian Ocean. Part I: Ocean dynamics, *J. Mar. Res.*, *40*, 157–176.

McPhaden, M. J., and X. Yu (1999), Equatorial waves and the 1997–1998 El Niño, *Geophys. Res. Lett.*, *26*(19), 2961–2964, doi:10.1029/1999GL004901.

McPhaden, M. J., et al. (2009), RAMA: The Research Moored Array for African-Asian-Australian Monsoon Analysis and Prediction, *Bull. Am. Meteorol. Soc.*, *90*, 459–480, doi:10.1175/2008BAMS2608.1.

Moore, D. W., and J. P. McCreary (1990), Excitation of intermediate-frequency equatorial waves at a western ocean boundary: With application to observations from the Indian Ocean, *J. Geophys. Res.*, *95*, 5219–5231, doi:10.1029/JC095iC04p05219.

Nagura, M., and M. J. McPhaden (2010a), Wyrtki Jet dynamics: Seasonal variability, *J. Geophys. Res.*, *115*, C07009, doi:10.1029/2009JC005922.

Nagura, M., and M. J. McPhaden (2010b), Dynamics of zonal current variations associated with the Indian Ocean dipole, *J. Geophys. Res.*, *115*, C11026, doi:10.1029/2010JC006423.

Philander, S. G. H. (1990), *El Niño, La Niña, and the Southern Oscillation*, Academic, London.

Reppin, J., F. A. Schott, and J. Fischer (1999), Equatorial currents and transports in the upper central Indian Ocean: Annual cycle and interannual variability, *J. Geophys. Res.*, *104*, 15,495–15,514, doi:10.1029/1999JC900093.

Reverdin, G. (1987), The upper equatorial Indian Ocean: The climatological seasonal cycle, *J. Phys. Oceanogr.*, *17*, 903–927, doi:10.1175/1520-0485(1987)017<0903:TUEIOT>2.0.CO;2.

Reverdin, G., and J. Luyten (1986), Near-surface meanders in the equatorial Indian Ocean, *J. Phys. Oceanogr.*, *16*, 1088–1100, doi:10.1175/1520-0485(1986)016<1088:NSMITE>2.0.CO;2.

Senan, R., D. Sengupta, and B. N. Goswami (2003), Intraseasonal "monsoon jets" in the equatorial Indian Ocean, *Geophys. Res. Lett.*, *30*(14), 1750, doi:10.1029/2003GL017583.

Sengupta, D., R. Seanan, and B. N. Goswami (2001), Origin of intraseasonal variability of circulation in the tropical central Indian Ocean, *Geophys. Res. Lett.*, *28*(7), 1267–1270, doi:10.1029/2000GL012251.

Sengupta, D., R. Senan, B. N. Gosawami, and J. Vialard (2007), Intraseasonal variability of equatorial Indian Ocean zonal currents, *J. Clim.*, *20*, 3036–3055, doi:10.1175/JCLI4166.1.

Vialard, J., S. S. C. Shenoi, J. P. McCreary, D. Shankar, F. Durand, V. Fernando, and S. R. Shetye (2009), Intraseasonal response of the northern Indian Ocean coastal waveguide to the Madden-Julian Oscillation, *Geophys. Res. Lett.*, *36*, L14606, doi:10.1029/2009GL038450.

Weisberg, R. H., and C. Wang (1997), Slow variability in the equatorial west-central Pacific in relation to ENSO, *J. Clim.*, *10*, 1998–2017, doi:10.1175/1520-0442(1997)010<1998:SVITEW>2.0.CO;2.

Yu, X., and M. J. McPhaden (1999), Seasonal variability in the equatorial Pacific, *J. Phys. Oceanogr.*, *29*, 925–947, doi:10.1175/1520-0485(1999)029<0925:SVITEP>2.0.CO;2.

Zhang, C. (2005), Madden-Julian Oscillation, *Rev. Geophys.*, *43*, RG2003, doi:10.1029/2004RG000158.

Zhang, X., and M. J. McPhaden (2006), Wind stress variations and interannual sea surface temperature anomalies in the eastern equatorial Pacific, *J. Clim.*, *19*, 226–241, doi:10.1175/JCLI3618.1.

M. J. McPhaden, Pacific Marine Environmental Laboratory, National Oceanic and Atmospheric Administration, 7600 Sand Point Way NE, Seattle, WA 98115, USA.

M. Nagura, Application Laboratory, Japan Agency for Marine-Earth Science and Technology, 3173-25 Showa-machi, Kanazawa-ku, Yokohama, Kanagawa 236-0001, Japan. (nagura@jamstec.go.jp)